# A LUT-based approach to estimate surface solar irradiance by combining MODIS and MTSAT data

Guanghui Huang,[1] Mingguo Ma,[1] Shunlin Liang,[2] Shaomin Liu,[3] and Xin Li[1]

Received 17 April 2011; revised 5 September 2011; accepted 6 September 2011; published 16 November 2011.

[1] In this paper, a new satellite-derived approach for obtaining instantaneous surface solar irradiance (SSI) by combining Moderate Resolution Imaging Spectroradiometer (MODIS) and Multifunctional Transport Satellite (MTSAT) data is presented and validated using one year pyranometer measurements from five stations in northern China. The approach is based on look-up tables created via comprehensive radiative transfer modeling to achieve high accuracy and high computational efficiency. The synergy of the multispectral sensor MODIS and the high-temporal-resolution geostationary satellite MTSAT enables the adequate use of multisource remote sensing information to determine the atmosphere and surface states, and thereby complements shortcomings of their own. Here we use MTSAT data to capture the changes of cloud fields in the atmosphere and use MODIS products to obtain the dynamic aerosol loading, water vapor content, surface reflectance, and other information. Meanwhile, on the basis of instantaneous retrieval results, the calculation of hourly average SSI is also explored. The preliminary validation demonstrates that both instantaneous and hourly SSIs can be produced accurately over northern China using this approach, and the retrieval quality of hourly SSI data is slightly better than that of instantaneous SSI data. However, in mountainous areas the results need further refinement.

**Citation:** Huang, G., M. Ma, S. Liang, S. Liu, and X. Li (2011), A LUT-based approach to estimate surface solar irradiance by combining MODIS and MTSAT data, *J. Geophys. Res.*, *116*, D22201, doi:10.1029/2011JD016120.

## 1. Introduction

[2] The Earth's surface radiation budget is an essential parameter for estimation of the surface energy budget and is used for various applications, including weather prediction, monitoring and analysis of climate, and terrestrial ecological and hydrological systems [*Bisht et al.*, 2005; *Oliphant et al.*, 2006]. As a particularly important component of the surface radiation budget, surface solar irradiance (SSI) is the primary source of energy for the Earth's surface; it controls the total energy exchange between the atmosphere and the land-ocean surface and also serves as a key driving force for evapotranspiration, plant growth, and related processes [*Pinker et al.*, 1995; *Roebeling et al.*, 2004; *Deneke et al.*, 2008; *Mueller et al.*, 2009]. Hence, SSI is of fundamental interest in many research fields and is an important variable for our understanding of the climate system and the processes and interactions taking place within it.

[3] SSI data with large geographical coverage (up to global) and high spatiotemporal resolution can be obtained from satellite data. This has been confirmed by many studies [e.g., reviews by *Schmetz*, 1989; *Pinker et al.*, 1995]. Estimating the surface solar radiation using satellite remote sensing techniques is essential not only for complementing the sparse network of surface station measurements, but also for verifying climate model output and reanalysis data. Radiances at the top of the atmosphere (TOA) observed by satellite instruments are modulated by the atmosphere and land surface and thus in return reflect certain information on atmospheric and Earth's surface states. This information is crucial for the retrieval of surface radiation. As early as 1964, *Fritz et al.* [1964] had already found that the correlation coefficient between satellite measurements of reflected solar radiation and pyranometer measurements at the ground was as high as 0.9. Since then, numerous approaches have been proposed to estimate the SSI from satellite radiances.

[4] One type of approach mainly uses atmospheric parameters (e.g., cloud properties) retrieved by different algorithms from multifarious satellites as inputs for a given radiative transfer model (RTM) to obtain surface solar fluxes. Such approaches require two independent steps. First, atmospheric state parameters need to be inverted from narrowband satellite radiances. Together with other climatology and ancillary data, these atmospheric state parameters are then used for RTM modeling to calculate the atmospheric flux transmittance. One example of this type of approach is the operational algorithm adopted by the International

[1]Cold and Arid Regions Environmental and Engineering Research Institute, Chinese Academy of Sciences, Lanzhou, China.
[2]Laboratory for Global Remote Sensing Studies, Department of Geography, University of Maryland, College Park, Maryland, USA.
[3]School of Geography, State Key Laboratory of Remote Sensing Science, Beijing Normal University, Beijing, China.


0148-0227/11/2011JD016120

Satellite Cloud Climatology Project (ISCCP) [*Zhang et al.*, 1995, 2004]. In this algorithm, ISCCP cloud climatology data sets as well as many ancillary data were exploited as the inputs of NASA Goddard Institute for Space Studies (GISS) general circulation model (GCM) radiation model [*Hansen et al.*, 1983, 2002] to produce global fluxes from surface to the TOA. Another example is the algorithm developed by *Bishop et al.* [1997], who utilized the total cloud amount and cloud optical depth (COD) from ISCCP as important input parameters for SSI calculations.

[5] Another type of approach, which directly establishes the parameterization scheme and/or look-up table (LUT) to link the SSI and satellite radiances were also frequently reported in the literature. One of the most famous of this type is the algorithm developed by *Pinker and Ewing* [1985] and *Pinker and Laszlo* [1992]. This algorithm was adopted by the Global Energy and Water Cycle Experiment (GEWEX) Surface Radiation Budget (SRB) project to routinely produce surface shortwave radiation data. It was also the basis for the first operational version of the CM-SAF (Satellite Application Facility on Climate Monitoring) SRB [*Hollmann et al.*, 2006]. The LUT-based eigenvector hybrid approach established by *Mueller et al.* [2009], which is the CM-SAF operational scheme for satellite-based SSI retrieval, and the operational scheme for estimating downward shortwave radiation from GMS 5 visible imagery developed by *Lu et al.* [2010] also belong to this type.

[6] In addition to the aforementioned approaches, there is a third type of method, which is more empirical and easier to operate. One prominent and widely used approach in this class is the Heliosat algorithm as well as its derivatives [*Cano et al.*, 1986; *Hammer et al.*, 2003; *Rigollier et al.*, 2004]. In these algorithms, a clear-sky model is used in advance to acquire surface solar radiation under supposedly cloud-free conditions. Then the cloud index, defined as the ratio of surface and TOA solar radiation, is determined with normalized reflectances from satellite images. Finally, the SSI values in all skies are calculated with these two terms. The Heliosat algorithm has been used in many European research projects, such as the Satel-Light project, which delivers valuable information to architects and other stakeholders, and the SoDa project, which aims to integrate databases on solar radiation and other related information [*Hammer et al.*, 2003]. Another similar algorithm is the Staylor algorithm, which is used by the GEWEX SRB project as a quality control algorithm [*Gupta et al.*, 2001] and is also one of the two algorithms chosen by the World Climate Research Program SRB project for generating SSI data from March 1985 to December 1998 [*Whitlock et al.*, 1995]. An intercomparsion on different algorithms for surface solar radiation based on Moderate Resolution Imaging Spectroradiometer (MODIS) data has been given in our previous work [*Huang et al.*, 2011], and we think that for multispectral remote sensing data such as MODIS, simple experiential algorithms are improper and a more refined algorithm needs to be developed.

[7] However, as indicated by *Deneke et al.* [2008], the experimental nature of many algorithms, the small number of overpasses of polar-orbiting satellite systems, the instability and disorder of previous atmospheric products based on various specific sensors or other means, and the coarse spatial and spectral resolutions of geostationary satellites have limited the satellite retrieval of SSI. Fortunately, this situation may change greatly if we combine advanced polar-orbiting satellite sensors data, especially MODIS products, with the next generation of geostationary meteorological satellite data. MODIS has 36 spectral bands covering the visible and infrared regions. After in-orbit operation, many inversion algorithms for atmospheric and land parameters had been refined by MODIS science team and diverse normative products had been produced routinely. These may provide a data source superior to widely used climatology data sets (e.g., for aerosol and water vapor). Moreover, geostationary satellites with higher temporal resolutions can satisfy the need for information on clouds, which strongly influence SSI estimation. Therefore, in this paper we try to develop a new retrieval algorithm based on a complicated RTM for SSI calculation, in which the increased information on the atmospheric state from new satellite systems can be adequately exploited. This is a crucial distinction between our algorithm and that developed by *Lu et al.* [2010], who use only GMS-5 geostationary satellite data.

[8] The primary objective of the new retrieval algorithm is to obtain high-quality surface solar radiation over northern China, and we strive to reach two distinct virtues. One is to exploit up-to-date remote sensing information and eliminate the need for ground information as much as possible; the other is to ensure both high accuracy and high computational efficiency. To preserve the algorithm's accuracy in theory, we do not import any parameterizations to reduce the RTM modeling magnitude, as was done by *Mueller et al.* [2009]. Furthermore, this complicated RTM-based approach allows us to acquire surface spectral solar irradiance, sequentially easily to calculate photosynthetically active radiation (PAR), ultraviolet (UV) or actinic fluxes, and even the vertical atmosphere shortwave radiation flux profiles from the surface to the TOA.

[9] The paper is organized as follows. Section 2 concisely describes the satellite and surface observational data we used. Section 3 covers the processes of this new algorithm in detail. Section 4 presents the validation result, our error analysis, and a detailed discussion. Finally, in section 5 we summarize our SSI retrieval approach.

## 2. Data

[10] Two types of satellite data were used in this study: polar-orbiting satellite products from multispectral MODIS, and geostationary meteorological satellite data from the Multifunctional Transport Satellite MTSAT1R. The former were selected to obtain certain atmospheric parameters that cannot be determined through the sparse geostationary satellite sensor bands. The latter were used to obtain cloud-fluctuating information that cannot be captured only from the low-frequency polar-orbiting satellite observations. In addition, some ancillary data were imported in order to improve the algorithm's performance, and surface pyranometer measurements were used to evaluate the algorithm's accuracy.

### 2.1. MODIS Data Products

[11] At present, there are 44 available standard MODIS data products that are being used by scientists from a variety of disciplines, including oceanography, biology, and atmospheric

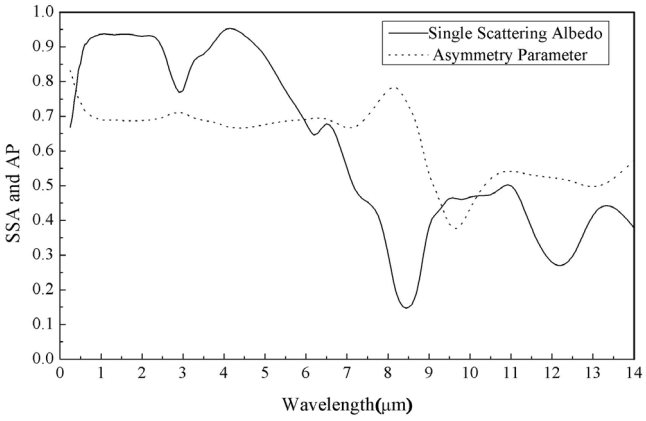


**Figure 1.** Single scattering albedo and asymmetry parameter derived from GADS summer data sets and considered as the representative case of northern China.

science. In this paper, MOD08_D3, MOD10C1, and MCD43C2 obtained from EOS Data Gateway were used. A brief description of these data products is given below.

[12] MOD08_D3 is the level-3 atmosphere daily global product that contains roughly 600 statistical data sets collected from the Terra platform. These data sets are derived from approximately 80 scientific parameters from level-2 MODIS atmosphere products (aerosol, water vapor, cloud, and atmosphere profiles) and are stored on an equal-angle latitude-longitude grid in hierarchical data format. MOD10C1 is the MODIS/Terra Snow Cover Daily L3 Global 0.05° Climate Modeling Grid (CMG) data set created by assembling MOD10A1 daily tiles and binning the 500 m cell observations to 0.05° spatial resolution of the CMG cell. It contains snow cover, quality assessment data, and corresponding metadata. We use it to obtain the information on cloud and snow percentages of CMG cells. MCD43C2 is an L3 0.05° CMG MODIS bidirectional reflectance distribution function (BRDF) albedo model parameters product produced by averaging snow-free quality 500 m BRDF parameters. It contains the weighting parameters of the BRDF models, which are elements of the derived surface albedo and directional reflectance [*Schaaf et al.*, 2002], such as the albedo (MCD43C3) and NBAR (MCD43C4) products.

### 2.2. MTSAT Satellite Data

[13] The Japan MTSAT series succeeded the Geostationary Meteorological Satellite (GMS) series as the next generation of satellites covering East Asia and the western Pacific. It currently fulfills two functions: a meteorological function and an aeronautical function. MTSAT1R, the first satellite of the MTSAT series, sits in geostationary orbit at 140°E. It has one visible and three infrared channels and can observe the Northern Hemisphere of the Earth every 30 min. The original nadir spatial resolution of visible channel is 1 km, but the data we used are the preprocessed products with 5 km spatial resolution.

### 2.3. Ancillary Data and Pyranometer Surface Measurements

[14] Different aerosol types always have distinctive optical properties (herein they are characterized by the single scattering albedo and asymmetry parameter) and strongly affect the surface incident direct and diffuse solar light proportion and magnitude [*Pilinis et al.*, 1995; *Mueller et al.*, 2009]. Unfortunately, these aerosol optical properties are not easy to determine only by satellite remote sensing techniques. Therefore, here the Global Aerosol Data Set (GADS) was employed.

[15] GADS is a revised version of the aerosol climatology data compiled by *d'Almeida et al.* [1991], which was also used in MODIS Collection 4 aerosol standard products [*Kaufman et al.*, 1997]. This data set is used mainly in climate modeling. For the entire globe, on a grid of 5° longitude-latitude, with seven differentiating height profiles for both summer and winter, the aerosol content at each grid point consists of 10 predefined aerosol components. Because our region of principal interest is northern China, the aerosol optical properties within the region of 100°E–120°E and 35°N–45°N for summer are averaged and treated as the representative aerosol optical properties (shown in Figure 1) in the present study. Moreover, the aerosol optical depth (AOD) from GADS will be treated as the default AOD to replace invalid MODIS retrieval values.

[16] The pyranometer data for validation come from five meteorological stations where the SSI is measured alongside other meteorological parameters. These stations are the Guantao and Daxing experimental stations in north China and the Yingke oasis station, Huazhaizi desert station, and A'rou freeze-thaw observation station in northwest China (Table 1). The latter three stations were built by Watershed Allied Telemetry Experimental Research (WATER) [*Li et al.*, 2009]. The specific SSI observation instruments are the CMP3 pyranometers provided by Kipp & Zonen. A CMP3 pyranometer consists of a housing, dome, cable, and thermopile sensor, which is coated with a black absorbent coating. The coating absorbs radiation and converts it to heat, and then a copper-constantan thermopile converts the resulting temperature difference to a voltage. Overall, the typical error is not expected to exceed 5%.

## 3. SSI Approach Description

[17] A flowchart illustrating the instantaneous SSI retrieval is presented in Figure 2. The algorithm can be divided into two different stages. First, we establish the

**Table 1.** Summary of the Five Meteorological Stations

| Site | Location | Latitude (deg) | Longitude (deg) | Altitude (m) | Landscape | Others |
|---|---|---|---|---|---|---|
| Guantao | North China | 116.427 | 39.621 | 30 | Field cropland | Haihe River basin |
| Daxing | North China | 115.127 | 36.515 | 20 | Cash cropland | Haihe River basin |
| Yingke oasis | Northwest China | 100.410 | 38.857 | 1519 | Cropland(maize) | Heihe River basin |
| Huazhaizi desert | Northwest China | 100.317 | 38.767 | 1726 | Desert steppe | Heihe River basin |
| A'rou freeze | Northwest China | 100.465 | 38.044 | 3033 | Alpine meadow | Heihe River basin |

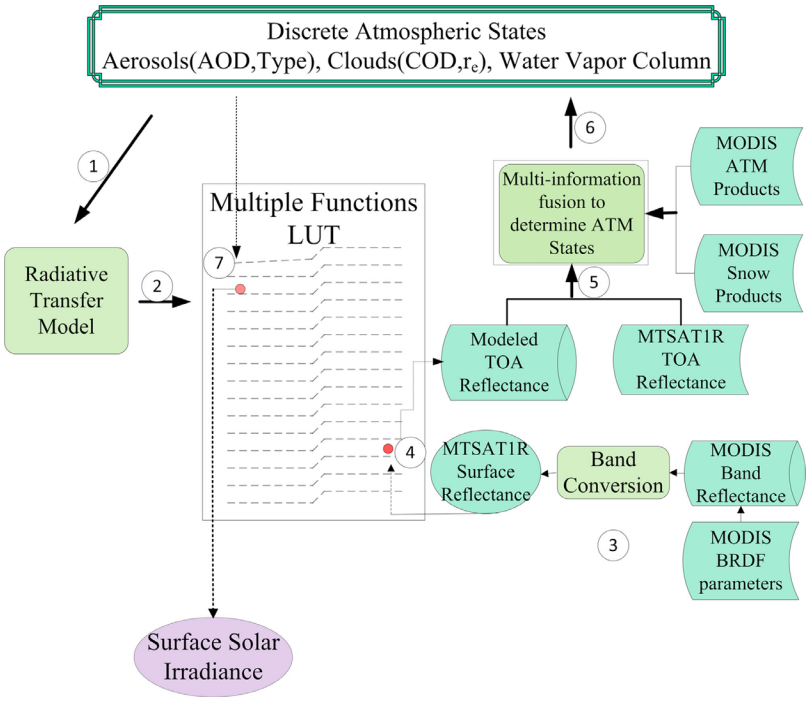


**Figure 2.** The basic algorithm flowchart of instantaneous SSI estimation.

LUTs by comprehensive RTM modeling for various discrete atmospheric states. Second, MODIS products and MTSAT1R data are integrated to determine the atmospheric states, and subsequently the SSI is estimated. To accurately determine atmospheric states, the surface states must be estimated in advance. Therefore, sections 3.1 and 3.2 describe the creation of LUTs for clear and cloudy skies; section 3.3 provides an approach to estimating surface reflectance and albedo; and section 3.4 describes specific instantaneous SSI retrieval processes. In addition, the calculation of hourly SSI is explored in section 3.5.

[18] Horizontal surface incident solar irradiance depends mainly on the atmospheric state, but also to a lesser extent on the surface properties. To calculate the surface incident solar irradiance denoted by the symbol $F_s$, we must know the atmospheric flux transmittance $T$, spherical albedo of the atmosphere $\overline{\rho}$, TOA irradiance $F_0$, and surface albedo $r_s$. They are linked by [*Liang*, 2004],

$$F_s(\mu_0,\Lambda) = \mu_0 F_0(\Lambda) T(\mu_0,\Lambda) + \frac{r_s(\Lambda)}{1 - r_s(\Lambda)\overline{\rho}(\Lambda)} \mu_0 F_0(\Lambda) T(\mu_0,\Lambda), \tag{1}$$

where $\mu_0$ is the cosine of the solar zenith angle (SZA) and $\Lambda$ denotes a certain spectral range. Strictly speaking, this equation applies only to monochromatic radiation. However, the resulting errors are small even if it is used over the entire solar spectrum. Different spectral ranges are used in the literature to define the SSI. In this study, it is specified in the range of 0.3–3 $\mu$m. To obtain the parameters in equation (1), the RTM must be run. Note that $F_0$ changes slightly with the Sun-Earth distance.

[19] Before running the RTM to create LUTs, it is critical to analyze the interaction between the atmospheric state, surface albedo, and SSI in order to minimize the RTM runs and optimize the distribution of grid points in the LUT. That is, a sensitivity study on the effects of the parameters on SSI must be done in advance. Fortunately, this has been performed and documented by other authors [*Li et al.*, 1993; *Mueller et al.*, 2009; *Lu et al.*, 2010] and also in our previous work.

### 3.1. Creating the LUT for Clear Skies

[20] For a Lambertian surface, the TOA apparent reflectance $\rho_{\mathrm{TOA}}$ can be calculated with the classical formula

$$\rho_{\mathrm{TOA}}(\mu_0,\mu,\varphi,\Lambda) = \rho_a(\mu_0,\mu,\varphi,\Lambda) + \frac{r_s(\Lambda)}{1 - r_s(\Lambda)\overline{\rho}(\Lambda)} \cdot T(-\mu_0,\Lambda) T(\mu,\Lambda), \tag{2}$$

in which $\rho_a$ is caused by the path radiance without surface contribution, $\mu$ is the cosine of the viewing zenith angle (VZA), $\varphi$ is the relative azimuth angle (RAA), and $T(-\mu_0)T(\mu)$ can be thought of as a two-way transmittance.

[21] In developing the LUT approach for clear skies, we focus on two atmospheric state parameters, aerosol optical depth and water vapor content. As a note of caution, hereafter discussions of the aerosols involved are based on the optical properties shown in Figure 1. Figure 3 (left) demonstrates the sensitivity of the MTSAT1R TOA visible band apparent reflectance (TOA-VIS-AR) to the AOD. It is found that the trend of the fluctuation of MTSAT1R TOA-VIS-AR with the AOD is complicated and relevant to surface reflectance. Hence, it is difficult to determine the land AOD using only the MTSAT1R visible band. On the other hand, MTSAT1R TOA-VIS-AR is largely insensitive to alterations in the atmospheric water vapor content (WVC). These facts

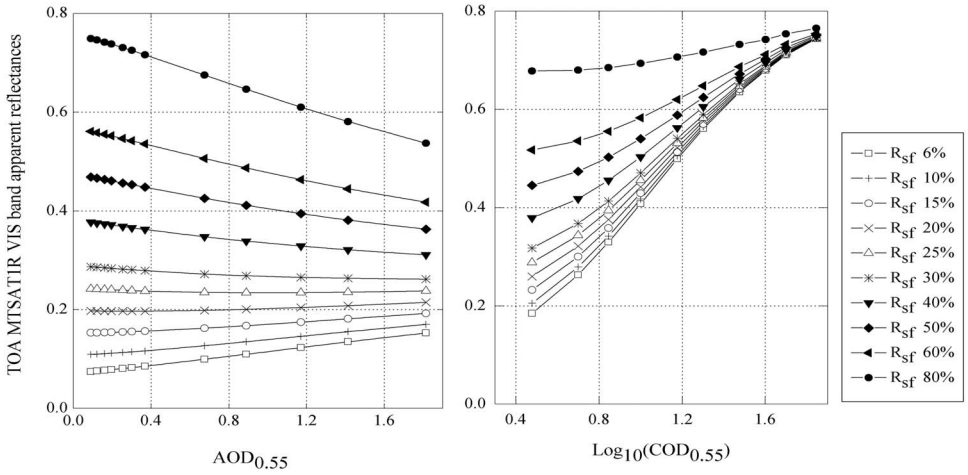


**Figure 3.** (left and right) Fluctuations of TOA MTSAT1R VIS band apparent reflectance with variations in aerosol and cloud optical depth (SZA = 45°, VZA = 90°, RAA = 0°). Curves are for different surface reflectances, ranging from 0.06 (bottom) to 0.8 (top).

are the most important causes why we introduce MODIS atmospheric products into the algorithm.

[22] Although for clear skies MTSAT1R TOA-VIS-AR values are not used directly for SSI retrieval, they are necessary for cloud detection by a threshold algorithm. Thus, the corresponding variables for the calculation of the modeled clear MTSAT1R TOA-VIS-AR are also preserved in the LUT. This means that all variables in equations (1) and (2) are tabulated off-line as functions of the AOD and WVC. To obtain those variables, the radiative transfer package MODTRAN [*Berk et al.*, 2000] is used in this study. For each grid point in the LUT, to minimize numerical noise, three surface reflectances (0.0, 0.5, and 0.8) are specified for the wave number interval ranging from 33,333 to 3333 in increments of 10 wave numbers. The MODTRAN-modeled TOA radiance at each increment for the three surface reflectances are integrated with MTSAT's spectral response function (SRF) to obtain three average TOA apparent reflectance values, and these apparent reflectances are used to solve for the quantities $\rho(\mu_0, \mu, \varphi, \Lambda)$, $\overline{\rho}\,(\Lambda)$, and $T(-\mu_0, \Lambda)T(\mu, \Lambda)$. Finally, $T(\mu_0, \Lambda)$ and $\overline{\rho}\,(\Lambda)$ for the entire SSI spectral segment as well as the above three variables are saved in the LUT (see Table 2).

[23] In the present study, MODTRAN built-in aerosol optical properties have been replaced with the aforementioned representative aerosols from GADS and the following values are used in the RTM simulations: SZA (0°, 10°, 20°, 30°, 40°, 45°, 50°, 55°, 60°, 65°, 70°, 75°, and 80°), VZA (0°, 15°, 30°, 40°, 50°, 55°, 60°, and 65°), RAA (0°, 30°, 60°, 90°, 120°, 150°, and 180°), AOD (0.09, 0.12, 0.16, 0.25, 0.37, 0.67, 1.17, 1.81, and 2.60) at 0.55 $\mu$m, and WVC (0.1, 0.5, 1.0, 1.5, 2.0, 2.5, and 5 cm). The impacts of other absorptive gases and ozone on SSI are considered marginal, and the default values in MODTRAN are used. Namely, they are not treated as variables in the LUT.

### 3.2. Creating the LUT for Cloudy Skies

[24] In the presence of clouds, an ideal one-dimensional (1-D) cloud field with varying CODs and an effective droplet radius of 10 $\mu$m [*Bishop and Rossow*, 1991; *Hu and Stamnes*, 1993; *Lohmann et al.*, 2006] are assumed to establish the cloudy-sky LUT. Ten $\mu$m is a typical average droplet radius of nonprecipitating water clouds. *Siegel et al.* [1999] and *Mueller et al.* [2009] both indicated that setting the effective radius to a value of 10 $\mu$m does not change the SSI results noticeably. Figure 3 (right) shows that a considerable portion of incident radiation can be reflected back into space with increasing COD, and for a surface reflectance of less than 0.5, the TOA reflectances are obviously greater than those under cloud-free conditions. This is the basis of the threshold algorithm that determines whether a given pixel is covered by clouds.

[25] Here another RTM called LibRadtran is used since it is more sophisticated than MODTRAN in terms of modeling the cloud field. LibRadtran is a library of radiative transfer routines and programs (B. Mayer et al., Library for radiative transfer calculations, edition 1.0 for libRadtran version 1.5-beta, 2010). It contains precomputed scattering parameters for a set of effective radii in a certain range using a Mie scattering code for spherical drop radii. The radiative

**Table 2.** A Typical LUT at a Specific Sun-Object-Viewer Geometry[a]

| COD | AOD | WVC (cm) | MTSAT VIS $\rho_a$ | MTSAT VIS $\overline{\rho}$ | MTSAT VIS $T(-\mu_0)T(\mu)$ | $T_{dir}$ | $T_{dif}$ | $\overline{\rho}$ |
|---|---|---|---|---|---|---|---|---|
| 0.000 | 0.902 | 0.1 | 0.040811 | 0.056338 | 0.808377 | 0.72703 | 0.10797 | 0.08238 |
| 0.000 | 0.902 | 0.5 | 0.040578 | 0.055794 | 0.794835 | 0.69209 | 0.10666 | 0.08468 |
| ⋮ | ⋮ | ⋮ | ⋮ | ⋮ | ⋮ | ⋮ | ⋮ | ⋮ |
| 70.00 | 0.324 | 2.5 | 0.789645 | 0.83583 | 0.005824 | 0.00000 | 0.06286 | 0.83471 |

[a]SZA = 50°, VZA = 60°, and RAA = 120°. $T_{\rm dir}$, $T_{\rm dif}$, and $\overline{\rho}$ denote the direct flux transmittance, diffuse flux transmittance, and atmospheric spherical albedo, respectively; for other symbols, please refer to equation (2).

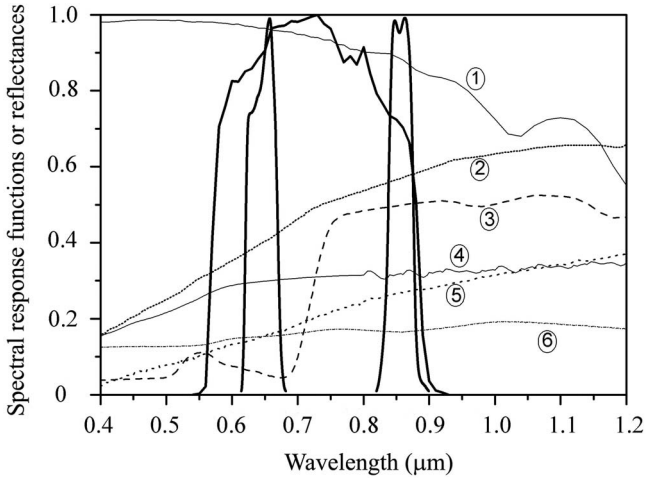


**Figure 4.** SRF of MTSAT1R VIS band, MODIS bands 1, 2, and six familiar surface reflectance spectra (1, medium granular snow; 2, dry grass; 3, grass; 4, construction; 5, brown loam; 6, quartzite). The broad, bold curve is the SRF of the MTSAT1R VIS; the two narrow curves are the SRFs of MODIS band 1 and band 2.

transfer equation solver is DISORT. Similar quantities are saved in the LUT as for clear-sky conditions (see Table 2) in the same geometric positions with varying CODs (1, 3, 5, 7, 10, 15, 20, 30, 40, 50, and 70). Since the influence of clouds on SSI is at a different level of magnitude compared with that of other atmospheric parameters, in cloudy skies the AOD and WVC are fixed at certain values.

### 3.3. Determination of Surface MTSAT1R VIS Band Reflectance and Albedo

[26] The underlying surface band reflectance and albedo may significantly affect the determination of COD over land and subsequent SSI retrieval, especially for low COD values. In the MODIS standard cloud product algorithm, the land cover type and ecosystem are used as predictors of spectral albedo [*Platnick et al.*, 2003]. However, here MCD43 BRDF-albedo products are directly used to obtain the surface reflectance and albedo in the MTSAT VIS band. Since there are discrepancies in the sensor SRF between MODIS and MTSAT, a conversion algorithm of surface band reflectance and albedo needs to be developed beforehand.

[27] The spectral response range of the MTSAT1R VIS band is 0.55~0.9 $\mu$m. This interval contains two intact MODIS bands that are symmetrically located at the two terminals, at which many surface reflectance curves exhibit different characteristics (Figure 4). This indicates that the MTSAT1R surface reflectance and albedo may be estimated accurately from the surface BRDF-albedo of the two MODIS bands.

[28] The conversion approach proposed by *Liang* [2000] is adopted. In this study, a total of 119 surface reflectance spectra, including soil (32), vegetation (30), man-made (19), rock (20), snow and frost (6), and water (3), mainly from the Atmosphere-Surface Turbulent Exchange Research Facility (ASTER) spectral library [*Baldridge et al.*, 2009], and 9 reflectance spectra extracted from the hyperspectral Hyperion imagery collected by Watershed Allied Telemetry Experimental Research (WATER) [*Li et al.*, 2009] are employed to represent the surface characteristics. A series of aerosol loadings (9), water vapor content (6) as well as SZAs (13) are inputted into the RTM to obtain surface spectral fluxes. Then sensor SRFs are integrated with the above surface fluxes and reflectance spectra to generate band reflectance/albedos. Regression analysis is conducted to generate the conversion formula.

[29] The simulated and fitted surface MTSAT1R VIS band reflectance and albedo values are presented in Figure 5; a summary of the fitted residuals is also included. The residual standard error (RSE), multiple $R^2$ values, and an analysis of the residual all reveal that this conversion is quite effective and the surface MTSAT1R VIS band reflectance and albedo can be accurately determined from two MODIS band reflectances and albedos. The resultant linear equation is

$$\alpha_{\mathrm{MTSATVIS}} = 0.5804\alpha_{\mathrm{MODISB1}} + 0.4273\alpha_{\mathrm{MODISB2}} - 0.0046, \quad (3)$$

where $\alpha_{\mathrm{MTSATVIS}}$, $\alpha_{\mathrm{MODISB1}}$, and $\alpha_{\mathrm{MODISB2}}$ are the band reflectance and albedo of MTSAT1R VIS, MODIS band 1, and MODIS band 2, respectively.

[30] The surface reflectance and albedo change with the solar elevation angle throughout the day. To obtain the dynamic surface reflectance and albedo, MCD43C2 products are utilized to reconstruct the surface reflectance, black-sky albedo, and white-sky albedo at any desired SZA and VZA. The kernel-driven linear BRDF model adopted by MODIS standard products is also used here. The following formula presents the most rudimentary portion of the operational MODIS BRDF algorithm [*Schaaf et al.*, 2002]:

$$R(\theta_0, \theta, \phi, \Lambda) = f_{\mathrm{iso}}(\Lambda) + f_{\mathrm{vol}}K_{\mathrm{vol}}(\theta_0, \theta, \phi, \Lambda) + f_{\mathrm{geo}}K_{\mathrm{geo}}(\theta_0, \theta, \phi, \Lambda) \quad (4)$$

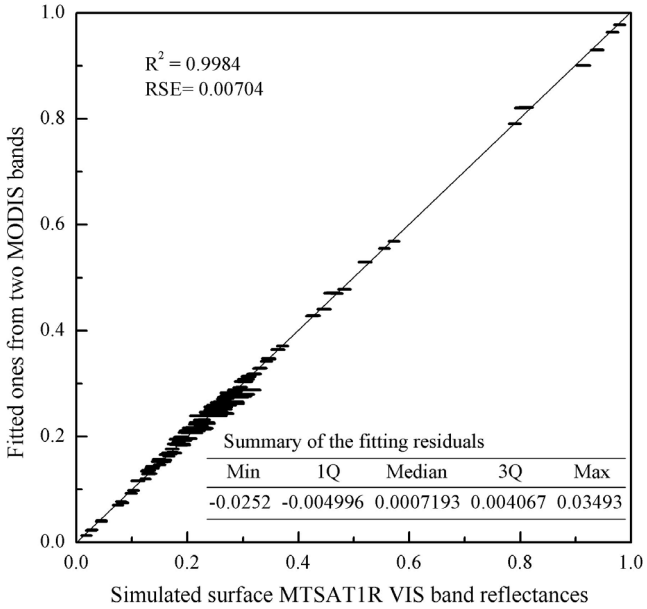


**Figure 5.** Simulated surface MTSAT VIS band reflectances as predicted by the two MODIS bands' reflectances.

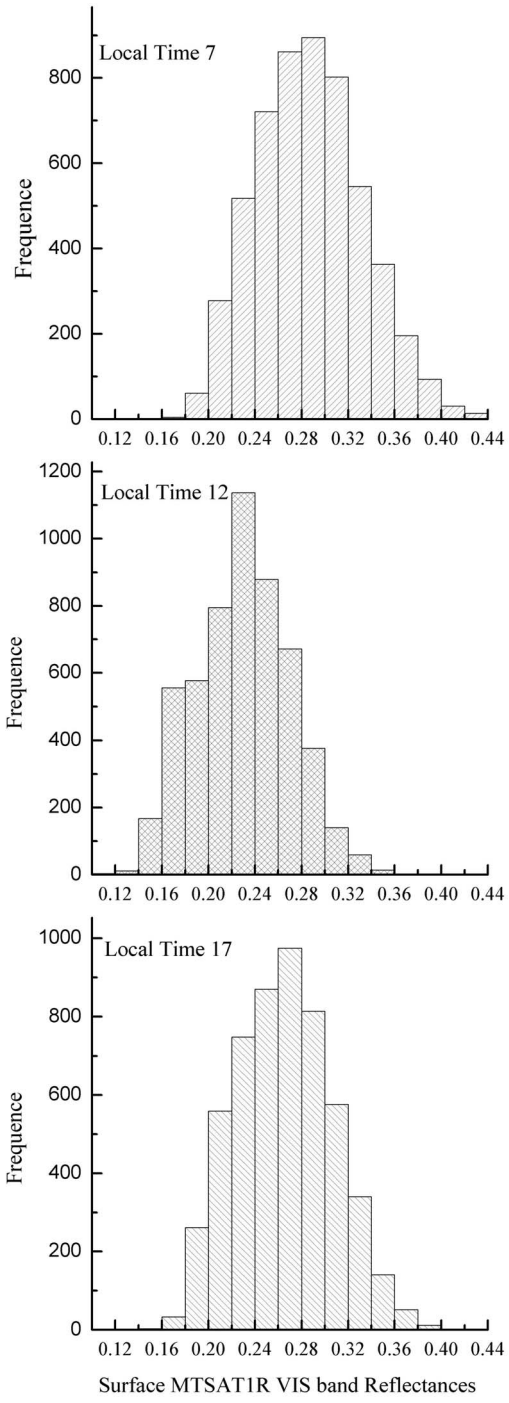


**Figure 6.** Histograms of surface MTSAT1R VIS band reflectances over one of our primary regions of interest, the Heihe river basin, China, at different local times (1 July 2009): (top) 7:00, (middle) 12:00, and (bottom) 17:00.

where $R$ is the bidirectional reflectance, $K_{vol}$ is the Ross thick kernel, $K_{geo}$ is the Li sparse kernel, and parameters $f_i$ are the kernel coefficients. We extract each set of three coefficient parameters as well as the quality flags for the MODIS 1, 2, and shortwave (0.3~5.0 $\mu$m) bands from MCD43C2. All cells marked as poor quality are excluded. The corresponding good parameters for MODIS bands 1 and 2 are used to calculate the surface band reflectance and white-sky albedo at one specific sun-object-viewer geometry (the specific calculation procedure can be found in other papers and thus is not repeated here). The band conversion approach described above is then used to generate the MTSAT1R VIS band reflectance and white-sky albedo under the same conditions. The three coefficient parameters for the shortwave bands are used to calculate the surface albedo $r_s$ in equation (1).

### 3.4. Instantaneous SSI Retrieval

[31] As soon as the LUT is established, the SSI as well as direct or diffuse solar irradiance can be expediently calculated by searching the LUT. Since direct or diffuse radiation may yield different light-use efficiencies, a number of global primary production models and global carbon cycle studies have treated them separately [*Gu et al.*, 2002]. Hence, direct and diffuse radiation will be calculated and output separately in our algorithm. In the following discussion, we take SSI retrieval as an example to explain the processes in detail.

[32] First, the MTSAT1R VIS band reflectance and white-sky albedo are computed using the approach described in section 3.3. The MTSAT1R VIS band white-sky albedo is especially critical for the determination of the COD because even a moderate COD may make the direct beam very weak. A case of surface reflectance retrieval over the Heihe river basin in northwest China is shown in Figure 6. From Figure 6 we can find that most of the surface reflectances are within 0.2–0.3. This further confirms that the MTSAT1R VIS band cannot be used to determine the atmospheric aerosol loadings because the TOA reflectances are not sensitive to the AOD in this interval (Figure 3).

[33] Second, for a given set of surface condition, the TOA reflectances at certain atmospheric states can be predicted using equation (2). The aerosol loadings are derived from the data sets "Corrected_Optical_Depth_Land" in the intraday MOD08D3 products. Subsequently, modeled TOA reflectances for clear skies at any specific geometry position can be obtained with the above calculated surface reflectances and albedos. Then the factual TOA reflectances observed by MTSAT1R are compared with the modeled ones to determine whether clouds exist. Because of the noises and calibration discrepancies of the sensors, in our present algorithm, four levels of confidence are given, namely "clear," "possibly clear," "possibly cloudy," and "cloudy." For the two intermediate situations, a simple spatial consistency check is conducted to refine the determination. Compared with operational cloud detection algorithms [*Rossow and Garder*, 1993; *Amato et al.*, 2008; *Ricciardelli et al.*, 2008], this scheme is simple and effective.

[34] Finally, for cells identified as clear, the LUTs are searched immediately to acquire the direct and diffuse flux transmittance according to the AOD and WVC from the MOD08D3 products. For cloudy cells, the LUTs are used first to calculate the modeled TOA reflectances with varying COD. Then the TOA reflectances observed by MTSAT1R are compared with the modeled ones to interpolate the cloud optical thickness. Finally, two flux transmittances are determined. Here a multidimensional linear interpolation technique is adopted in the operational algorithm.

[35] After all atmospheric variables and surface reflectance and albedo values are obtained; equation (1) is utilized to calculate the incident SSI. The direct and diffuse solar irradiances can also be calculated in the same way. Note that, as in most RTMs [*Liang*, 2004], the irradiance resulting from the interactions between the surface and atmosphere is considered diffuse light.

[36] However, for cells covered by snow, the aforementioned algorithm will fail. Therefore, an alternative algorithm is employed in this situation. MOD10C1 snow cover products are preprocessed to obtain spatiotemporally continuous surface daily snow cover maps. A series of processes similar to those described by *Dozier et al.* [2008] were adopted. Then, for cells flagged as "snow," the cloud properties are extracted from a supplementary cloud data set of the MODIS cloud products, which is retrieved by the combination of the MODIS bands 6 (1.6 $\mu$m) and 7 (2.1 $\mu$m) where the snow reflectance is low. Finally, the SSI over the snowy surface is calculated separately.

### 3.5. Hourly Average SSI Estimation

[37] The instantaneous SSI can be very useful for evapotranspiration estimation and many ecosystem models. For more applications, however, the average SSI over a specific time interval is of interest. In particular, the hourly average SSI is widely used. To compute the hourly average SSI, the average atmospheric flux transmittance (AFT) must first be calculated. This quantity is defined as

$$\widetilde{T} = \frac{\int_{t1}^{t2} T(t)\mathrm{F}_0\mu_0(t)}{\int_{t1}^{t2} \mathrm{F}_0\mu_0(t)} \tag{5}$$

and can be approximately estimated by

$$\widetilde{T} \approx \frac{\sum_{i=1}^{n} T_i\mu_i}{\sum_{i=1}^{n} \mu_i}, \tag{6}$$

where $n$ is the number of satellite observations per unit time, and $\mu_i$ is the solar zenith angle at one specific time of satellite observation. Thus, the hourly average AFT is the weighted average of the instantaneous AFT and $\mu_0$ is the weighting factor [*Deneke et al.*, 2008]. Cumulative sums of the TOA fluxes can be obtained by an analytic equation,

$$F_{\mathrm{STOA}} = \mathrm{F}_0 \int_{t1}^{t2} [a\cos(\omega t + f) + b]\mathrm{d}t = \mathrm{F}_0\left(\frac{a}{\omega}\sin(\omega t + f) + bt\right)\Big|_{t1}^{t2}, \tag{7}$$

$$a = \cos(\mathrm{lat})\cos(\delta), \tag{8}$$

$$b = \sin(\mathrm{lat})\sin(\delta), \tag{9}$$

$$f = \omega(-20 + 0.0666667\mathrm{lon} + 3.81972\eta), \tag{10}$$

$$\omega = 2 \times \pi/24, \tag{11}$$

where $\delta$ is the solar declination, $\eta$ is the solar time lag, and the other two parameters are the latitude and longitude (in radians). The mean TOA flux in 1 h can be calculated. As for the other atmospheric variables in equation (1), arithmetic mean values may be sufficient. The hourly average SSI values are obtained sequentially.

## 4. Results

[38] The determination of cloud properties becomes unreliable at large SZAs; hence, we do not produce any SSI data for satellite measurements for which SZAs are larger than 80°. In this section, the algorithm discussed above is evaluated using data from five stations in northern China. Next, error analysis is conducted, and the aspects that induce larger inaccuracy and require further investigation are also presented.

### 4.1. Algorithm Evaluation with Pyranometer Measurements

[39] This section compares the retrieval instantaneous and hourly SSI values with the ground pyranometer measurements. For each station, the mean SSI values from the southerly neighboring 2 × 3 satellite pixel windows were extracted and considered as the satellite-retrieved site SSI values. Station measurements recorded every 10 or 30 min were interpolated or averaged to obtain the corresponding site SSI values (instantaneously and hourly). The two SSI values for each site were compared here to evaluate the algorithm's accuracy, though a more valuable scheme on the validation of SSI had been implicated by *Deneke et al.* [2009]. The selected periods are from September 2008 to August 2009.

[40] Because of the notable differences between ground and satellite observations, both spatial and temporal mismatches could occur, and it may be difficult to characterize the correlation between them using traditional statistical analysis. Therefore, as analyzed by *Liang et al.* [2006], a robust regression analysis technique, called the least trimmed squares regression, is adopted. In our study, the largest squared residuals are trimmed by 5%; that is, the regression method minimizes the sum of the smallest 95% squared residuals. Some common error evaluation indices and robust regression analysis results are listed in Tables 3a and 3b. The rough error distributions are shown in Figure 7.

[41] Both instantaneous and hourly SSI results are given separately for a summer half year and a winter half year because of their distinct retrieval quality (see Tables 3a and 3b). The evaluation reveals that this approach can accurately predict the surface incident solar radiation even under cloudy conditions. The mean correlation coefficient is as high as 0.958, and the root-mean-square error (RMSE) is generally less than 100 W/m$^2$. This indicates a very high correlation and good agreement between the retrieved and measured values. Moreover, the retrieval performance is appreciably better at the two stations in north China than at the three in northwest China for cloudy skies, but the inverse is true for clear skies. Among the five meteorological stations, the retrieval quality at the A'rou freeze station is significantly poorer than that at the others because it has more days of snow coverage. The statistics in Tables 3a and 3b also show that retrieval in the summer half year outper-

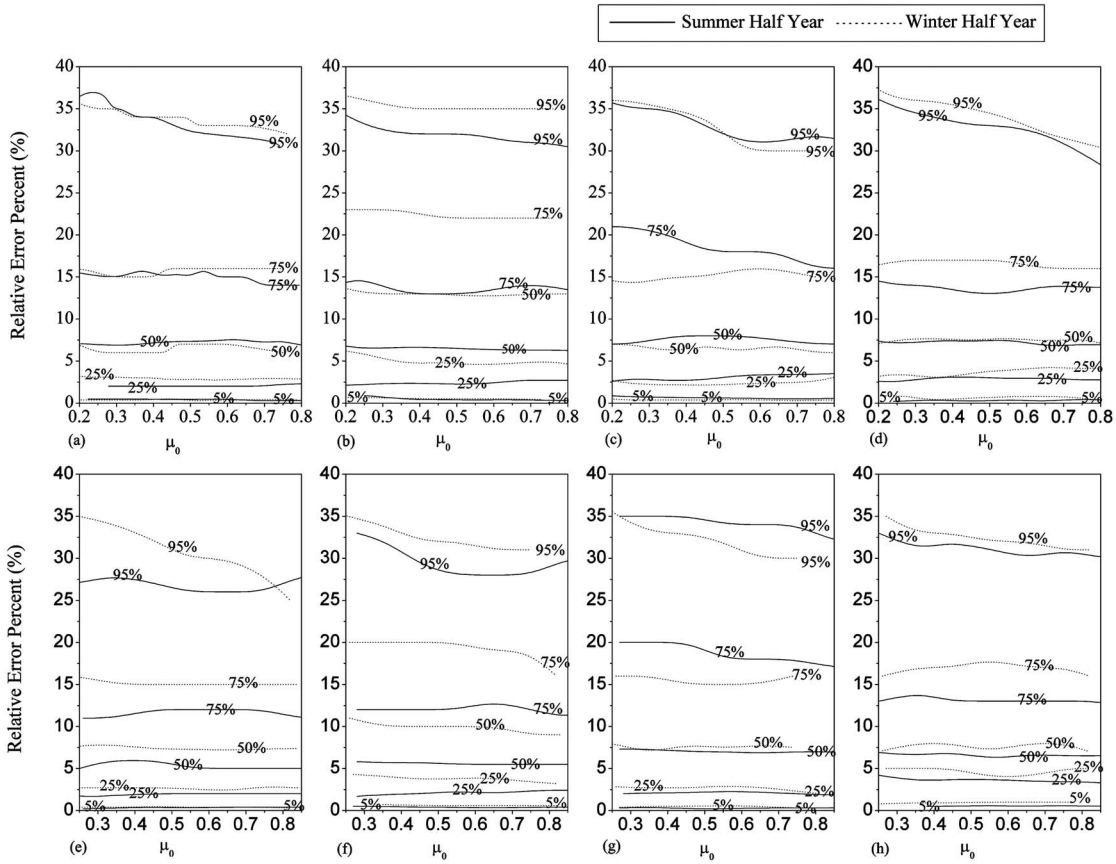


**Figure 7.** Percentiles of instantaneous and hourly SSI relative error as a function of $\mu_0$: (a) Guantao instantaneous, (b) Daxing instantaneous, (c) Yingke oasis instantaneous, (d) Huazhaizi desert instantaneous, (e) Guantao hourly, (f) Daxing hourly, (g) Yingke oasis hourly, (h) Huazhaizi desert hourly.

forms that in the winter half year. Possible explanations for this situation will be presented and explored in sections 4.2 and 4.3.

[42] Relative error percentiles can depict a detailed deviation curve between retrieved and measured values. Here the retrieval error percentiles of both the instantaneous and hourly values as functions of $\mu_0$ are represented in Figure 7. Owing to the effects of snow coverage and other causes (see section 4.3), the results of the A'rou freeze station require further improvement and are not shown in Figure 7. In addition to the above conclusions, Figure 7 also shows that half of the retrieval errors are below 7%, and 75% of them are below 16% at the four stations. The $\mu_0$ dependence of the retrieval errors is inconspicuous, and only at larger errors (95th percentile) a slight decrease of retrieval error with increasing $\mu_0$ is visible. In addition, two noteworthy features

**Table 3a.** Summary of Common Error Evaluation Indices and Robust Regression Analysis at the Five Stations for Instantaneous SSIs[a] ($W/m^2$)

| | | | | | LTS Regression Analysis | | | |
|---|---|---|---|---|---|---|---|---|
| Stations | Mean | Bias | MRE[b] (%) | RMSE | Slope | Intercept | Scale of the Residuals | Robust Multiple $R^2$ |
| | | | | *Spring-Summer* | | | | |
| Guantao | 426.2 | 4.1 | 13.1 | 77.7 | 1.052 | −22.6 | 62.6 | 0.943 |
| Daxing | 418.7 | 13.8 | 15.7 | 95.3 | 1.084 | −46.2 | 68.6 | 0.924 |
| Yingke oasis | 475.9 | 7.8 | 17.4 | 115.1 | 1.095 | −46.6 | 85.9 | 0.906 |
| Huazhaizi desert | 488.3 | −6.2 | 15.1 | 103.4 | 1.072 | 25.5 | 77.2 | 0.919 |
| A'rou freeze | 445.5 | −16.9 | 24.6 | 136.5 | 1.143 | −48.4 | 108.9 | 0.842 |
| | | | | *Fall-Winter* | | | | |
| Guantao | 303.2 | 6.3 | 14.6 | 60.6 | 0.996 | −9.50 | 50.0 | 0.909 |
| Daxing | 295.3 | 14.7 | 19.7 | 72.9 | 1.020 | −29.6 | 55.5 | 0.879 |
| Yingke oasis | 371.1 | −18.6 | 14.8 | 78.8 | 1.012 | 9.6 | 62.2 | 0.884 |
| Huazhaizi desert | 406.2 | −49.6 | 19.3 | 110.8 | 1.092 | 16.5 | 79.8 | 0.887 |
| A'rou freeze | 403.2 | −62.8 | 23.1 | 123.1 | 1.060 | 12.3 | 90.4 | 0.853 |

[a]SSIs measured in $W/m^2$.
[b]Mean relative error (MRE) is defined as $\frac{100}{N}\sum_{i=1}^{N}|1-\frac{y_r}{y_o}|$, where $N$ is the total number, $y_r$ and $y_o$ are the retrieved and observed SSI, respectively.

**Table 3b.** Corresponding Summary for Hourly Averaged SSIs[a]

| Stations | Mean | Bias | MRE[b] (%) | RMSE | LTS Regression Analysis | | | |
|---|---|---|---|---|---|---|---|---|
| | | | | | Slope | Intercept | Scale of the Residuals | Robust Multiple $R^2$ |
| *Spring-Summer* | | | | | | | | |
| Guantao | 456.4 | 3.6 | 12.5 | 76.9 | 1.085 | −37.5 | 61.2 | 0.941 |
| Daxing | 448.4 | 14.0 | 13.8 | 85.4 | 1.103 | −57.2 | 65.5 | 0.931 |
| Yingke oasis | 506.9 | 4.69 | 15.7 | 103.8 | 1.133 | −71.2 | 78.0 | 0.915 |
| Huazhaizi desert | 521.4 | −8.1 | 14.2 | 95.5 | 1.127 | −44.9 | 77.2 | 0.920 |
| A'rou freeze | 475.9 | −16.2 | 21.4 | 119.2 | 1.174 | −68.6 | 98.7 | 0.861 |
| *Fall-Winter* | | | | | | | | |
| Guantao | 333.4 | 4.2 | 13.6 | 60.4 | 1.018 | −13.8 | 49.7 | 0.902 |
| Daxing | 319.5 | 15.7 | 17.5 | 66.7 | 1.050 | −39.2 | 54.9 | 0.880 |
| Yingke oasis | 400.2 | −23.8 | 12.7 | 68.6 | 1.030 | 6.95 | 53.8 | 0.899 |
| Huazhaizi desert | 434.6 | −48.9 | 17.7 | 101.2 | 1.086 | 16.2 | 78.9 | 0.909 |
| A'rou freeze | 435.8 | −57.4 | 20.2 | 112.7 | 1.026 | 33.5 | 88.4 | 0.801 |

[a]SSIs measured in $W/m^2$.
[b]Mean relative error (MRE) is defined as $\frac{100}{N}\sum_{i=1}^{N}|1-\frac{y_r}{y_o}|$, where $N$ is the total number, $y_r$ and $y_o$ are the retrieved and observed SSI, respectively.

are visible: First, the accuracy of the winter half year at the Daxing station is obviously worse than that of the others. Second, the accuracy of the summer half year is generally higher than that of the winter half year, but at the Yingke oasis station the opposite trend is apparent. Next, we investigate this abnormality.

[43] Further investigation on the results at Yingke oasis station shows that the retrieved SSI values are much higher

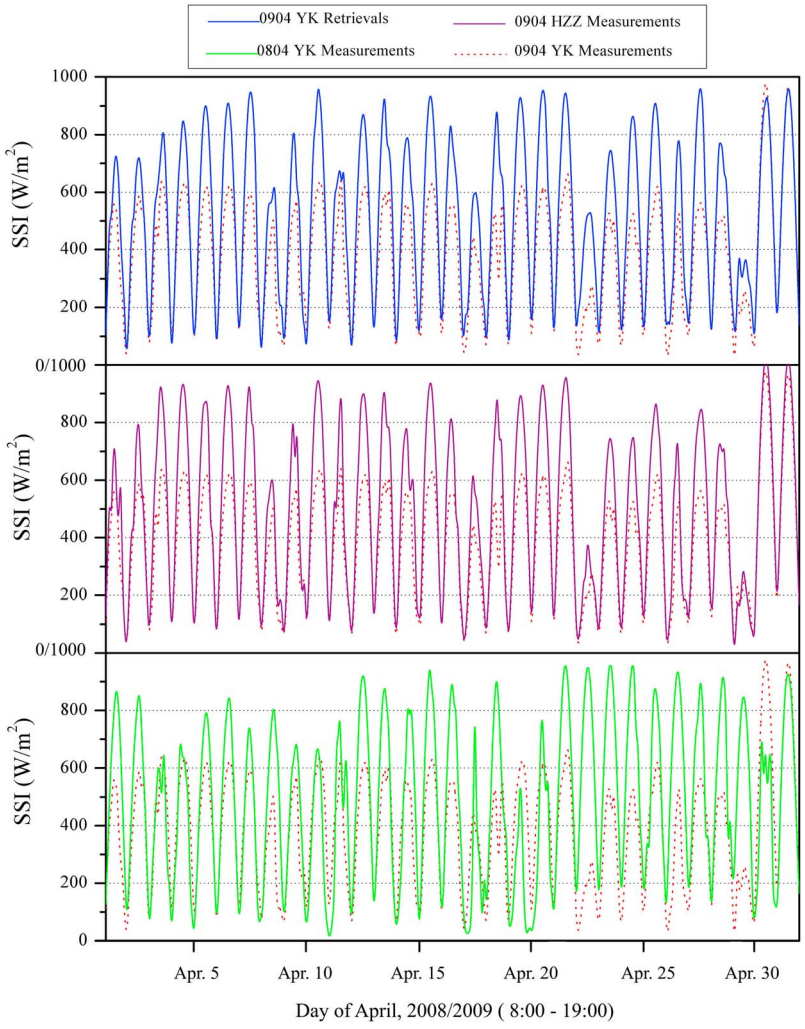


**Figure 8.** (top) Partially suspicious surface measurements at Yingke oasis station (YK) in the summer half year of 2009, comparing them with measurements from the Huazhaizi desert station (middle) for the same period and from YK for the same period in another year (bottom) (see the text for details).

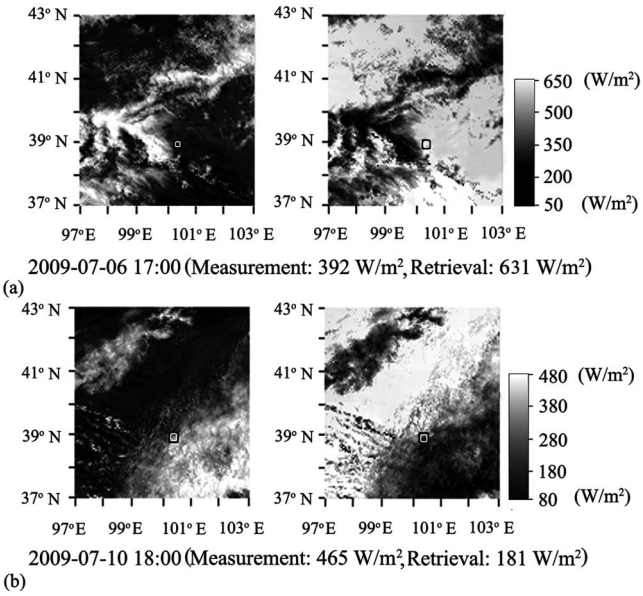


**Figure 9.** Two representative mismatches between satellite and ground-based observations over the neighborhood of the Heihe River basin ((left) MTSAT1R VIS band TOA apparent reflectance; (right) corresponding retrieved instantaneous SSIs). The squares mark the location of the Yingke oasis station.

than the pyranometer measurements from early March to early May 2009. Even if there are no clouds, the deviations frequently exceed 150 W/m$^2$. Apparently, such large errors should not occur normally. To identify the causes of this problem, a comparative investigation is conducted. The surface measurements from this period are compared with those during the same period at the Huazhaizi desert station, which is only a few dozen kilometers away from the Yingke oasis station, and those from the corresponding period in 2008. Figure 8 shows the comparative results of partial data (1 April through 2 May). The April 2009 measurements from the Yingke oasis station are much lower than the other measurements and the retrieved data, whereas in May they agree well. Therefore, we strongly suspect that the measurements made during this period at the Yingke oasis station are incorrect. It is very likely that the outside glass dome of the pyranometer was contaminated, resulting in the lower observed values.

### 4.2. Error Analysis

[44] Unlike the ground-based fixed-point measurements, what the satellite observations provide are the integrated effects of a certain spatial coverage. Observational differences caused by the mismatch in sampling scale seem unavoidable and are amplified by the presence of broken clouds. This situation will make the pyranometer data and satellite-derived estimates incompatible, especially at larger SZAs and VZAs. We found that in the Heihe river basin, this is obvious because all the VZAs of MTSAT1R are greater than 60° herein. When the SZA and VZA are both large and in approximately opposite directions, e.g., in the afternoon in the Heihe river basin in summer (Figure 9), the effects will be doubled.

[45] Grouping all the retrieved and measured SSIs by month we found that in clear skies some degree of overestimation appears in the winter half year, especially in December and January. The positive bias of 20–60 W/m$^2$ in January at different stations under cloud-free conditions indicates that the summer aerosol type used by this algorithm may be not appropriate for winter. According to the aerosol composition provided by GADS, the winter aerosols in northern China contain a large proportion of sootlike aerosol components compared with the summer aerosols. In consequence, the forward scattering radiation of the winter aerosol type is not as strong as that of the summer aerosol type. Figure 10 describes the different effects of the two aerosol types on surface solar direct and diffuse irradiance (refer to section 2.3 and Figure 1 on the summer aerosol type). For an SZA of 60° at moderate aerosol loadings, the deviations of surface diffuse irradiance from these two aerosol types has been up to 30 W/m$^2$ and will become greater with the increasing AOD. This could be the main reason that the errors are so large at the Daxing station in the winter half year (see Figures 7b and 7f). Therefore, dynamic adjustment of the aerosol type is likely to further reduce the algorithm error during clear-sky conditions. This improvement is expected to be done in our planned studies. In addition, many overestimated SSI values appear in July and August at the Guantao and Daxing stations. One possible explanation is that in this period the water vapor in the atmospheric surface layer was supersaturated (even fog appears), but this situation is not considered in our algorithm.

[46] Another error source comes from the snow covered surfaces, as clearly noted by *Deneke et al.* [2008]. First, short episodes of snow falling and melting are not always correctly monitored by the MODIS snow cover products. Once the pixels of these high TOA reflectances are mistakenly identified as clouds, underestimation is inevitable.

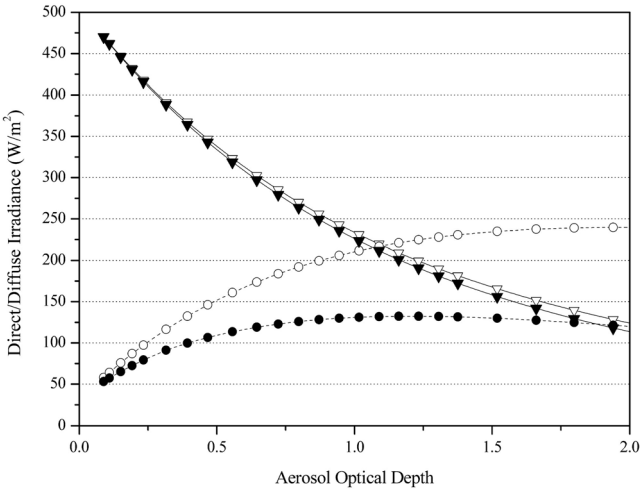


**Figure 10.** Differences in surface solar direct and diffuse irradiances caused by different aerosol types at a SZA of 60° (open triangles, direct irradiance from summer aerosol type; solid triangles, direct irradiance from winter aerosol type; open circles, diffuse irradiance from summer aerosol type; solid circles, diffuse irradiance from winter aerosol type).

Second, the supposition of water clouds is improper in the presence of snow and can aggravate the underestimation of SSI again. These are the primary reasons for the negative bias of the three stations in the Heihe river basin in the winter half year. The supplementary algorithm for snow covered surfaces needs further improvement. The degraded accuracy is so significantly evident that new strategies may be considered in future studies [*Li et al.*, 2007; *Pinker et al.*, 2007]. If snow covered conditions are excluded, the all-year biases of instantaneous SSI are 4.9 W/m$^2$ (Guantao), 11.2 W/m$^2$ (Daxing), 8.3 W/m$^2$ (Yingke oasis), 1.7 W/m$^2$ (Huazhaizi desert) and −12.5 W/m$^2$ (A'rou freeze) respectively, and the corresponding RMSEs are 68.5 W/m$^2$, 84 W/m$^2$, 88.2 W/m$^2$, 89.4 W/m$^2$, and 97.8 W/m$^2$. Accordingly, the all-year hourly SSI drops to a range of −9.6–10 W/m$^2$ at different stations, and the RMSE is less than 91 W/m$^2$. Currently available global satellite-estimated surface downwelling shortwave irradiance data sets include GEWEX-SRB, ISCCP-FD, and CERES-FSW. *Sheng et al.* [2010] accessed these three data sets with ground measurements collected at 36 globally distributed sites from 2000 to 2002 and reported an $R^2$ of 0.69–0.83, a bias of −5.5–29.7 W/m$^2$, and an RMSE of 101.7–123.2 W/m$^2$. Our algorithm obviously performs better than the above three data sets, considering their longer time scale.

[47] Last but not least, the quality of the MODIS products is questionable, especially in mountainous areas. Owing to the dependency of the algorithm's accuracy on the input data, this problem at least contributes to the poorer retrieval qualities at the A'rou freeze station. Strong orographic effects complicate the satellite inversion process because the satellite TOA reflectances are modulated twice by them. In particular, in the presence of thin clouds whose optical depth is less than 5, even small surface reflectance errors can yield the contradictory conclusions regarding whether pixels are covered by clouds. Consequently, erroneous atmospheric properties may be determined and large SSI retrieval errors are caused. Moreover, the differences in the sensor calibration of MODIS and MTSAT1R also affect the determination of atmospheric states, and the corresponding errors will be propagated into the SSI retrieval process.

## 5. Discussion

[48] At present, the hypothesis of a plane-parallel atmosphere is universal in surface solar radiation estimations regardless of which type of method, parameterization or 1-D radiative transfer simulation, is adopted. For absolutely clear weather conditions, this does not substantially affect SSI estimation. However, in the presence of clouds, this hypothesis may be totally wrong because many studies have revealed that the anisotropy of clouds is very strong [*Wyser et al.*, 2002, 2005; *Nauss et al.*, 2005]. Because the spatial structures of clouds are difficult to detect by remote sensing, the application of 3-D radiative transfer models is very sporadic in current solar radiation estimations. Therefore, 1-D RTM-based algorithms for SSI are known to contain biases due to 3-D radiative effects, whereas such effects can be implicitly accounted for in some empirical algorithms. Moreover, since the TOA reflectances are determined by two-way transfer processes of lights, satellite-derived SSI retrieval is subject to the impacts of variability in cloud fields and sun-object-viewer geometry. This may be a shortcoming of the current, truly theoretical approaches relative to empirical approaches.

[49] Fortunately, the errors caused by these effects would apparently be reduced if the time scales of the surface radiation calculation were expanded, e.g., for daily, monthly, or yearly averages SSIs. The order of accuracy of these qualities is generally comparable to that of first-class pyranometers, which has been reported by other researchers [*Deneke et al.*, 2008; *Mueller et al.*, 2009].

[50] In fact, our approach includes a common LUT approach for cloud optical depth, and, strictly speaking, it is intended mainly for plane-parallel liquid water clouds. Therefore, there are some cases for which the assumptions underlying the retrieval are not met. This problem is obvious at the A'rou freeze station, where semitransparent clouds are often observed. The large reflectance of this type of cloud, which is not accounted for in the retrieval algorithm, is attributed to liquid water clouds. This causes an overestimation of a cloud's optical thickness and an underestimation of solar irradiance. This could be another reason for the large negative bias at the A'rou freeze station. Thus, a specific improvement related to this aspect seems very necessary.

[51] However, the sparse number of sensor channels in current geostationary meteorological satellites hinders the development of more refined and quantitative SSI retrieval algorithms. Although the Spinning Enhanced Visible and Infrared Imager (SEVIRI) sensors aboard European meteorological satellites have up to 12 channels, the Visible and Infrared Spin Scan Radiometer (VISSR) sensor covering the China region, either from the MTSAT series or the FY series of the China Meteorological Administration, still has only 4 or 5 channels, and only one is in the solar spectral region. This increases the difficulty of determining atmospheric states. In particular, the absence of the aerosol-sensitive blue band makes the estimation of land aerosols very challenging (Figure 3); on the other hand, without the 1.6 $\mu$m infrared band, cloud detection and inferences of a cloud thermodynamic phase become difficult. Perhaps a more sophisticated algorithm could be developed if more advanced sensor instruments are launched in the future.

## 6. Conclusions

[52] The paper describes and evaluates a new approach to estimating surface solar irradiance (SSI) by combining MODIS and MTSAT1R data. This new approach is based completely on 1-D radiative transfer modeling without any empirical parameterizations, although this induces a huge number of RTM runs. Its features are that the virtues of polar-orbiting and geostationary meteorological satellites are adequately combined, and the newest satellite remote sensing products are imported in the calculation of surface solar radiation. The use of an efficient look-up table scheme enables us to theoretically keep the accuracy as high as possible.

[53] Meanwhile, the hourly SSI is also calculated using the obtained instantaneous values of atmosphere flux transmittance, atmospheric spherical albedo, and surface albedo in 1 h. The performed validation demonstrates that the retrievals of both instantaneous and hourly SSIs are

reasonably accurate and this approach is promising. The order of accuracy of this method is comparable to that of those reported by *Deneke et al.* [2008] and *Mueller et al.* [2009]. Although some shortcomings are still required to be addressed, we are confident that the reliable and quality surface solar radiation data can be produced in most regions of northern China by this approach. Moreover, the paper discusses error sources in detail and mentions the future strategies for error rectification.

[54] Considering the high temporal and spatial resolutions of MTSAT1R data, the outputs of this approach can serve as an excellent source of information on surface solar radiation in addition to the traditional network of surface measurements. However, as we discussed above, the accuracy will be reduced dramatically if the approach is used in mountainous areas or over snow covered surfaces. This situation will be difficult to change before the appearances of more advanced sensors on geostationary meteorological satellite platforms.

[55] **Acknowledgments.** The authors would like to thank the WATER program and the investigators of the five stations that provided in situ measurements for our validation; the ASTER Spectral Library, GADS, and LibRadtran, for their open, easy, and free web access to the high-quality data set and software package we required; and anonymous reviewers for their valuable comments. This work was supported by the Main Direction Program of Knowledge Innovation of the Chinese Academy of Sciences (grant KZCX2-EW-312), the National High-Tech Program (863) of China (grant 2009AA122104), and Knowledge Innovation Project of the Chinese Academy of Sciences (grant KZCX2-YW-Q10-1).

## References

Amato, U., A. Antoniadis, V. Cuomo, L. Cutillo, M. Franzese, L. Murino, and C. Serio (2008), Statistical cloud detection from SEVIRI multispectral images, *Remote Sens. Environ.*, *112*(3), 750–766, doi:10.1016/j.rse.2007.06.004.

Baldridge, A. M., S. J. Hook, C. J. Grove, and G. Rivera (2009), The ASTER spectral library version 2.0, *Remote Sens. Environ.*, *113*(4), 711–715, doi:10.1016/j.rse.2008.11.007.

Berk, A., et al. (2000), MODTRAN 4 User's Manual, user's manual, Air Force Res. Lab., Hanscom AFB, Mass.

Bishop, J. K. B., and W. B. Rossow (1991), Spatial and temporal variability of global surface solar irradiance, *J. Geophys. Res.*, *96*(C9), 16,839–16,858, doi:10.1029/91JC01754.

Bishop, J. K. B., W. B. Rossow, and E. G. Dutton (1997), Surface solar irradiance from the International Satellite Cloud Climatology Project 1983–1991, *J. Geophys. Res.*, *102*(D6), 6883–6910, doi:10.1029/96JD03865.

Bisht, G., V. Venturini, S. Islam, and L. Jiang (2005), Estimation of the net radiation using MODIS (Moderate Resolution Imaging Spectroradiometer) data for clear sky days, *Remote Sens. Environ.*, *97*(1), 52–67, doi:10.1016/j.rse.2005.03.014.

Cano, D., J. M. Monget, M. Albuisson, H. Guillard, N. Regas, and L. Wald (1986), A method for the determination of the global solar radiation from meteorological satellite data, *Sol. Energy*, *37*(1), 31–39, doi:10.1016/0038-092X(86)90104-0.

d'Almeida, G., P. Koekpe, and E. Shettle (1991), *Atmospheric Aerosols: Global Climatology and Radiative Characteristics*, A. Deepak, Hampton, Va.

Deneke, H. M., A. J. Feijt, and R. A. Roebeling (2008), Estimating surface solar irradiance from METEOSAT SEVIRI-derived cloud properties, *Remote Sens. Environ.*, *112*(6), 3131–3141, doi:10.1016/j.rse.2008.03.012.

Deneke, H. M., W. H. Knap, and C. Simmer (2009), Multiresolution analysis of the temporal variance and correlation of transmittance and reflectance of an atmospheric column, *J. Geophys. Res.*, *114*, D17206, doi:10.1029/2008JD011680.

Dozier, J., T. H. Painter, K. Rittger, and J. E. Frew (2008), Time-space continuity of daily maps of fractional snow cover and albedo from MODIS, *Adv. Water Resour.*, *31*(11), 1515–1526, doi:10.1016/j.advwatres.2008.08.011.

Fritz, S., P. Krishna Rao, and M. Weinstein (1964), Satellite measurements of reflected solar energy and energy received at the ground, *J. Atmos. Sci.*, *21*(2), 141–151, doi:10.1175/1520-0469(1964)021<0141:SMORSE>2.0.CO;2.

Gu, L., D. Baldocchi, S. B. Verma, T. A. Black, T. Vesala, E. M. Falge, and P. R. Dowty (2002), Advantages of diffuse radiation for terrestrial ecosystem productivity, *J. Geophys. Res.*, *107*(D6), 4050, doi:10.1029/2001JD001242.

Gupta, S., D. Kratz, P. Stackhouse, and A. Wilber (2001), The Langley Parameterized Shortwave Algorithm (LPSA) for surface radiation budget studies, *NASA Tech. Pap., 2001-211272*, 31 pp.

Hammer, A., D. Heinemann, C. Hoyer, E. Lorenz, R. Muller, and H. G. Beyer (2003), Solar energy assessment using remote sensing technologies, *Remote Sens. Environ.*, *86*(3), 423–432, doi:10.1016/S0034-4257(03)00083-X.

Hansen, J., G. Russell, D. Rind, P. Stone, A. Lacis, S. Lebedeff, R. Reudy, and L. Travis (1983), Efficient three-dimensional global models for climate studies: Models I and II, Mon. *Weather Rev.*, *111*(4), 609–662, doi:10.1175/1520-0493(1983)111<0609:ETDGMF>2.0.CO;2.

Hansen, J., et al. (2002), Climate forcings in Goddard Institute for Space Studies SI2000 simulations, *J. Geophys. Res.*, *107*(D18), 4347, doi:10.1029/2001JD001143.

Hollmann, R., R. W. Muller, and A. Gratzki (2006), CM-SAF surface radiation budget: First results with AVHRR data, *Adv. Space Res.*, *37*(12), 2166–2171, doi:10.1016/j.asr.2005.10.044.

Hu, Y., and K. Stamnes (1993), An accurate parameterization of the radiative properties of water clouds suitable for use in climate models, *J. Clim.*, *6*(4), 728–742.

Huang, G., S. Liu, and S. Liang (2011), Estimation of net surface shortwave radiation from MODIS data, *Int. J. Remote Sens.*, *32*(19), 1–22.

Kaufman, Y. J., D. Tanre, L. A. Remer, E. F. Vermote, A. Chu, and B. N. Holben (1997), Operational remote sensing of tropospheric aerosol over land from EOS-MODIS, *J. Geophys. Res.*, *102*(D14), 17,051–17,067, doi:10.1029/96JD03988.

Li, X., R. T. Pinker, M. M. Wonsick, and Y. Ma (2007), Toward improved satellite estimates of short-wave radiative flux—Focus on cloud detection over snow: 1. Methodology, *J. Geophys. Res.*, *112*, D07208, doi:10.1029/2005JD006698.

Li, X., et al. (2009), Watershed Allied Telemetry Experimental Research, *J. Geophys. Res.*, *114*, D22103, doi:10.1029/2008JD011590.

Li, Z., H. G. Leighton, K. Masuda, and T. Takashima (1993), Estimation of Shortwave flux absorbed at the surface from TOA reflected flux, *J. Clim.*, *6*, 317–330, doi:10.1175/1520-0442(1993)006<0317:EOSFAA>2.0.CO;2.

Liang, S. (2000), Narrowband to broadband conversions of land surface albedo. I. Algorithms, *Remote Sens. Environ.*, *76*(1), 213–238.

Liang, S. (2004), *Quantitative Remote Sensing of Land Surfaces*, 534 pp., John Wiley, Hoboken, N. J.

Liang, S., T. Zheng, R. Liu, H. Fang, and S. Tsay (2006), Estimation of incident photosynthetically active radiation from Moderate Resolution Imaging Spectrometer data, *J. Geophys. Res.*, *111*, D15208, doi:10.1029/2005JD006730.

Lohmann, S., C. Schillings, B. Mayer, and R. Meyer (2006), Long-term variability of solar direct and global radiation derived from ISCCP data and comparison with reanalysis data, *Sol. Energy*, *80*(11), 1390–1401, doi:10.1016/j.solener.2006.03.004.

Lu, N., R. Liu, J. Liu, and S. Liang (2010), An algorithm for estimating downward shortwave radiation from GMS-5 visible imagery and its evaluation over China, *J. Geophys. Res.*, *115*, D18102, doi:10.1029/2009JD013457.

Mueller, R., C. Matsoukas, A. Gratzki, H. Behr, and R. Hollmann (2009), The CM-SAF operational scheme for the satellite based retrieval of solar surface irradiance–A LUT based eigenvector hybrid approach, *Remote Sens. Environ.*, *113*(5), 1012–1024, doi:10.1016/j.rse.2009.01.012.

Nauss, T., A. A. Kokhanovsky, T. Y. Nakajima, C. Reudenbach, and J. Bendix (2005), The intercomparsion of selected cloud retrieval algorithms, *Atmos. Res.*, *78*(1–2), 46–78, doi:10.1016/j.atmosres.2005.02.005.

Oliphant, A., C. Susan, B. Grimmond, H. P. Schmid, and C. Wayson (2006), Local-scale heterogeneity of photosynthetically active radiation (PAR), absorbed PAR and net radiation as a function of topography, sky condition and leaf area index, *Remote Sens. Environ.*, *103*(3), 324–337, doi:10.1016/j.rse.2005.09.021.

Pilinis, C., S. N. Pandis, and J. H. Seinfeld (1995), Sensitivity of direct climate forcing by atmospheric aerosols to aerosol size and composition, *J. Geophys. Res.*, *100*, 18,739–18,754, doi:10.1029/95JD02119.

Pinker, R. T., and J. A. Ewing (1985), Modeling surface solar radiation: Model formulation and validation, *J. Appl. Meteorol.*, *24*(5), 389–401, doi:10.1175/1520-0450(1985)024<0389:MSSRMF>2.0.CO;2.

Pinker, R. T., and I. Laszlo (1992), Modeling surface solar irradiance for satellite applications on a global scale, *J. Appl. Meteorol.*, *31*(2), 194–211, doi:10.1175/1520-0450(1992)031<0194:MSSIFS>2.0.CO;2.

Pinker, R. T., R. Frouin, and Z. Li (1995), A review of satellite methods to derive surface shortwave irradiance, *Remote Sens. Environ.*, *51*(1), 108–124, doi:10.1016/0034-4257(94)00069-Y.

Pinker, R. T., X. Li, W. Meng, and E. A. Yegorova (2007), Toward improved satellite estimates of short-wave radiative flux—Focus on cloud detection over snow: 2. Results, *J. Geophys. Res.*, *112*, D09204, doi:10.1029/2005JD006699.

Platnick, S., M. D. King, S. A. Ackerman, W. P. Menzel, B. A. Baum, J. C. Reidi, and R. A. Frey (2003), The MODIS cloud products: Algorithms and examples from terra, *IEEE Trans. Geosci. Remote Sens.*, *41*(2), 459–473, doi:10.1109/TGRS.2002.808301.

Ricciardelli, E., F. Romano, and V. Cuomo (2008), Physical and statistical approaches for cloud identification using Meteosat Second Generation-Spinning Enhanced Visible and Infrared Imager Data, *Remote Sens. Environ.*, *112*(6), 2741–2760, doi:10.1016/j.rse.2008.01.015.

Rigollier, C., M. Lefèvre, and L. Wald (2004), The method Heliosat-2 for deriving shortwave solar radiation from satellite images, *Sol. Energy*, *77*(2), 159–169, doi:10.1016/j.solener.2004.04.017.

Roebeling, R. A., E. V. Putten, G. Genovese, and A. Rosema (2004), Application of Meteosat derived meteorological information for crop yield predictions in Europe, *Int. J. Remote Sens.*, *25*, 5389–5401, doi:10.1080/01431160410001705024.

Rossow, W. B., and L. C. Garder (1993), Cloud detection using satellite measurements of infrared and visible radiance for ISCCP, *J. Clim.*, *6*(12), 2341–2369, doi:10.1175/1520-0442(1993)006<2341:CDUSMO>2.0.CO;2.

Schaaf, C. B., et al. (2002), First operational BRDF, albedo nadir reflectance products from MODIS, *Remote Sens. Environ.*, *83*(1–2), 135–148, doi:10.1016/S0034-4257(02)00091-3.

Schmetz, J. (1989), Towards a surface radiation climatology: Retrieval of downward irradiance from satellites, *Atmos. Res.*, *23*(3–4), 287–321, doi:10.1016/0169-8095(89)90023-9.

Sheng, G., S. Liang, K. Wang, and L. Li (2010), Assessment of three satellite-estimated land surface downward shortwave radiation datasets, *IEEE Trans. Geosci. Remote Sens.*, *7*(4), 776–780, doi:10.1109/LGRS.2010.2048196.

Siegel, D., T. K. Westberry, and J. C. Ohlmann (1999), Cloud color and ocean radiant heating, *J. Clim.*, *12*(4), 1101–1116, doi:10.1175/1520-0442(1999)012<1101:CCAORH>2.0.CO;2.

Whitlock, C. H., et al. (1995), First global WCRP shortwave surface radiation budget data set, *Bull. Am. Meteorol. Soc.*, *76*(6), 905–922, doi:10.1175/1520-0477(1995)076<0905:FGWSSR>2.0.CO;2.

Wyser, K., W. O'Hirok, C. Gautier, and C. Jones (2002), Remote sensing of surface solar irradiance with corrections for 3-D cloud effects, *Remote Sens. Environ.*, *80*(2), 272–284, doi:10.1016/S0034-4257(01)00309-1.

Wyser, K., W. O'Hirok, and C. Gautier (2005), A simple method for removing 3-D radiative effects in satellite retrievals of surface irradiance, *Remote Sens. Environ.*, *94*(3), 335–342, doi:10.1016/j.rse.2004.10.003.

Zhang, Y., W. Rossow, and A. Lacis (1995), Calculation of surface and top of atmosphere radiative fluxes from physical quantities based on ISCCP data sets: 1. Method and sensitivity to input data uncertainties, *J. Geophys. Res.*, *100*(D1), 1149–1165, doi:10.1029/94JD02747.

Zhang, Y., W. Rossow, A. Lacis, V. Oinas, and M. Mishchenko (2004), Calculation of radiative fluxes from the surface to top of atmosphere based on ISCCP and other global data sets: Refinements of the radiative transfer model and the input data, *J. Geophys. Res.*, *109*, D19105, doi:10.1029/2003JD004457.

G. Huang, X. Li, and M. Ma, Cold and Arid Regions Environmental and Engineering Research Institute, Chinese Academy of Sciences, 322 Dong-Gang West Rd., Lanzhou, Gansu 730000, China. (luckhgh@lzb.ac.cn)

S. Liang, Laboratory for Global Remote Sensing Studies, Department of Geography, University of Maryland, College Park, MD 20742, USA.

S. Liu, School of Geography, State Key Laboratory of Remote Sensing Science, Beijing Normal University, Beijing 100875, China.